

# Adaptive low Mach number simulations of nuclear flames

J. B. Bell, M. S. Day, and C. A. Rendleman  
Center for Computational Sciences and Engineering  
Lawrence Berkeley National Laboratory  
Berkeley, CA, 94720

S. E. Woosley and M. A. Zingale  
Department of Astronomy and Astrophysics  
University of California at Santa Cruz  
Santa Cruz, CA, 95064

March 20, 2003

## Abstract

We introduce a numerical model for the simulation of nuclear flames in Type Ia supernovae. This model is based on a low Mach number formulation that analytically removes acoustic wave propagation while retaining the compressibility effects resulting from nuclear burning. The formulation presented here represents a generalization to an arbitrary eos of low Mach number models used in combustion that are based on an ideal gas approximation. The low Mach number formulation permits time steps that are controlled by the advective time scales resulting in a substantial improvement in computational efficiency compared to a compressible formulation. We briefly discuss the basic discretization methodology for the low Mach number equations and their implementation in an adaptive projection framework. We present validation computations in which the computational results from the low Mach number model are compared to a compressible code and present an application of the methodology to the Landau-Darrieus instability of a carbon flame.

## 1 Introduction

Currently, the accepted model for Type Ia supernovae is the explosion of a carbon-oxygen white dwarf. Observational evidence is inconsistent with the nuclear burning occurring in a prompt detonation mode. Detailed computations show that a detonation predicts excess amounts of iron and fails to account for significant amounts of intermediate mass elements observed in the spectra of supernovae events. For this reason, it is believed that at least the initial phases are governed by the propagation of constant-pressure deflagrations. However, to obtain the energy generation rate needed to explode the star the deflagration must be dramatically accelerated relative to the laminar flame speed of the burning front. The recent review article by Hillebrandt and Niemeyer [15] provides an excellent discussion of the issues.

Within the star there are numerous mechanisms that have the potential to accelerate a deflagration wave. Landau-Darrieus [10,18] instabilities can lead to wrinkling of the flame [5]. Because the lighter ash lies below the heavier carbon-oxygen fuel, the flame interface is also subject to Rayleigh-Taylor and Kelvin-Helmholtz instabilities. Finally, the flame can be accelerated by interaction with turbulence arising from convective instabilities within the flame as well as turbulence generated by the deflagration itself.

Efforts focused on understanding the role of the different types of instabilities on accelerating a nuclear flame have generated substantial interest in computational studies of flame microphysics. Several authors have performed simulations in both two and three dimensions based on representing the flame as an interface propagating through the media, see Hillebrandt and Niemeyer [15] for a discussion of this literature. It has

also become possible to perform detailed direct numerical simulations in 2D and 3D that fully resolve the relevant burning and diffusive length scales. Simulations of this type, based on solving the reacting compressible flow equations are presented by Niemeyer and Hillebrandt [21], Khokhlov [16], Niemeyer and Hillebrandt [22], and Niemeyer et al. [20].

Although these types of simulation have been able to provide substantial insight into the dynamics of nuclear deflagrations, they are limited in terms of both the spatial extent that can be modeled and the computational expense associated with long time integrations. The use of modern adaptive mesh methodologies such as FLASH [7, 13] can be used to extend the size of the system that can be modeled; however, temporal integration remains a problem. The issue arises because the flame phenomena being studied propagate at speeds less than 1% of the sound speed in the star. Thus, time step limitations based on acoustic Courant-Friedrich-Levy (CFL) considerations severely limit the time step relative to the velocity of the flame.

Our goal in this paper is to introduce a low Mach number formulation of nuclear flames that alleviates the acoustic time step constraint. This approach, based on low Mach number asymptotics, uses a projection formulation coupled with higher-order Godunov advective differencing that allows time-steps based on advection speeds rather than acoustic speeds. This type of approach was first used for combustion by Rehm and Baum [24] and was derived from low Mach number asymptotics by Majda and Sethian [19]. For problems in combustion, governed by an ideal gas equation of state, the low Mach number approach has seen substantial development and has been successfully applied to simulation of laminar and turbulent flames in two and three dimensions. The methodology presented here generalizes the approach of Day and Bell [11] to the nuclear deflagration regime. In particular, we discuss the extension of the low Mach number methodology to degenerate equations of state typical of stellar environments. Day and Bell [11] also provides a survey of other approaches to low Mach number combustion modeling. For applications of this approach see Bell et al. [3] and Bell et al. [4].

In the next section we discuss the basic equations and introduce the low Mach number model. In section 3 we discuss the basic projection algorithm and sketch its incorporation into an adaptive mesh refinement algorithm. Section 4 presents a validation of the basic by comparison with detailed compressible computations and presents an initial application of the method to the study of a Landau-Darrieus instability in two dimensions. In the final section we discuss potential application of this approach to more detailed study of nuclear flame acceleration mechanisms.

## 2 Low Mach number model

The low Mach number model is derived from the compressible flow equations using asymptotic analysis. These equations describe conservation of mass, momentum and energy augmented with species equations for the isotopes present in the flame. For the stellar conditions typical of C + O flames we are considering here, the Lewis number, which is the ratio of energy transport to species diffusion, is  $O(10^7)$  and the Prandtl number, which is the ratio of fluid viscosity to energy transport, is  $O(10^{-5})$ . Under these conditions, the flow is well approximated by the system (see, for example, Timmes and Woosley [26])

$$\begin{aligned}\frac{\partial \rho}{\partial t} + \nabla \cdot \rho U &= 0 \\ \frac{\partial \rho U}{\partial t} + \nabla \cdot (\rho U U + p) &= \rho \vec{g} \\ \frac{\partial \rho E}{\partial t} + \nabla \cdot (\rho U E + p U) &= \nabla \cdot (\kappa \nabla T) + \rho U \cdot \vec{g} - \rho q_k \dot{\omega}_k \\ \frac{\partial \rho X_k}{\partial t} + \nabla \cdot \rho U X_k &= \rho \dot{\omega}_k\end{aligned}$$

Here,  $\rho$ ,  $U$ ,  $T$  and  $p$  are the density, velocity, temperature, and pressure, respectively, and  $E = e + U \cdot U/2$  is the total energy with  $e$  representing the internal energy. In addition,  $X_k$  is the abundance of the  $k^{\text{th}}$  isotope, with associated production rate  $\dot{\omega}_k$  and energy release  $q_k$ . Finally,  $\vec{g}$  is the gravitational force and  $\kappa$  is the

thermal conductivity. (We note that the assumptions that fluid viscosity and species diffusion are zero can be easily relaxed, see Day and Bell [11]).

For the stellar conditions being considered here the pressure contains contributions from ions, radiation, and electrons. (See Kippenhahn and Weigert [17] for a discussion of equations of state for stellar matter.) Thus,

$$p = p_{\text{ion}} + p_{\text{rad}} + p_{\text{ele}} \quad (1)$$

with

$$p_{\text{ion}} = \frac{\rho k T}{\bar{A} m_p} \quad , \quad p_{\text{rad}} = a T^4 / 3$$

and  $p_{\text{ele}}$  is the contribution to the thermodynamic pressure due to fermions. In these expressions,  $m_p$  is the mass of the proton,  $a$  is related to the Stefan-Boltzmann constant  $\sigma = ac/4$ ,  $c$  is the speed of light,  $1/\bar{A} = \sum_k X_k/A_k$ , and  $k$  is Boltzmann's constant. We note that pressure is of the form  $p = p(\rho, T, X_k)$ . The ionic component has the form associated with an ideal gas but the radiation and electron pressure components do not.

As a prelude to developing the low Mach number equations, we first rewrite the energy equation in terms of the enthalpy,  $h = e + p/\rho$

$$\rho \frac{Dh}{Dt} - \frac{Dp}{Dt} = \nabla \cdot \kappa \nabla T - \sum_k \rho q_k \dot{\omega}_k$$

For the low Mach number asymptotic analysis, we introduce scaled coordinates in which the time scale is proportional to the spatial scale times the advective velocity scale. In this scaling, we expand pressure and velocity in Mach number,  $M = U/c_s$ , ( $c_s$  is the sound speed),

$$p(x, t) = p_0(t) + Mp_1(t) + M^2\pi(x, t)$$

with a similar equation for  $U(x, t)$ . Substituting these expansions in  $M$  into the equations of motion given above, retaining highest order terms in  $M$  results in  $p_1(t) = 0$  and a modified momentum equation:

$$\frac{\partial \rho U}{\partial t} + \nabla \cdot \rho U U = -\nabla \pi + \rho \vec{g}. \quad (2)$$

Thus, the pressure is decomposed into a thermodynamic component,  $\pi$ , that depends only on time and a perturbation component that is  $O(M^2)$ . For the low Mach number model, we ignore the  $O(M^2)$  effects on the thermodynamics. For simplicity, in this paper we will assume that the nuclear flame occurs in an open environment under constant pressure so that the thermodynamic pressure is, in fact, a constant which we denote as  $p_0$ . With this assumption, the enthalpy equation reduces to

$$\frac{\partial \rho h}{\partial t} + \nabla \cdot (\rho U h) = \nabla \cdot \kappa \nabla T - \sum_k \rho q_k \dot{\omega}_k \quad (3)$$

The enthalpy and momentum equations combined with the species equations (and conservation of mass) describe the evolution of the low Mach number system. However, this evolution is also constrained by the equation of state. We will now show that this constraint is equivalent to a constraint on the divergence of the velocity field. If we differentiate the equation of state along particle paths we obtain

$$0 \equiv \frac{Dp}{Dt} = \frac{\partial p}{\partial \rho} \frac{D\rho}{Dt} + \frac{\partial p}{\partial T} \frac{DT}{Dt} + \sum_k \frac{\partial p}{\partial X_k} \frac{DX_k}{Dt} \quad .$$

Combining this equation with the mass conservation equation, we obtain

$$\nabla \cdot U = \frac{1}{\rho \frac{\partial p}{\partial \rho}} \left( \frac{\partial p}{\partial T} \frac{DT}{Dt} + \sum_k \frac{\partial p}{\partial X_k} \frac{DX_k}{Dt} \right)$$

To complete the specification of the low Mach number model, we need to derive the temperature evolution equation. We note that although the thermodynamic variables are most naturally expressed here in terms of  $\rho$ ,  $T$ , and  $X_k$ , for this derivation, it is more convenient to express the thermodynamics in terms of  $p$ ,  $T$  and the  $X_k$ . With this dependence, differentiating the enthalpy equation we have

$$\frac{Dh}{Dt} = \frac{\partial h}{\partial T} \bigg|_{p, X_k} \frac{DT}{Dt} + \frac{\partial h}{\partial p} \bigg|_{T, X_k} \frac{Dp}{Dt} + \sum_k \frac{\partial h}{\partial X_k} \bigg|_{p, T, X_{j, j \neq k}} \frac{DX_k}{Dt}$$

After substituting from the above equations and using the low Mach number condition on  $p$  we have

$$\rho c_p \frac{DT}{Dt} = \nabla \cdot \kappa \nabla T - \sum_k \rho (q_k + \xi_k) \dot{\omega}_k \quad (4)$$

where  $\xi_k = \frac{\partial h}{\partial X_k} \bigg|_{p, T, X_{j, j \neq k}}$ , and  $c_p = \frac{\partial h}{\partial T} \bigg|_{p, X_k}$  is the specific heat at constant pressure.

Substituting this into the above equation for  $\nabla \cdot U$  yields an expression for a constraint on the advective flow velocities:

$$\nabla \cdot U = \frac{1}{\rho \frac{\partial p}{\partial \rho}} \left( \frac{1}{\rho c_p} \frac{\partial p}{\partial T} \left( \nabla \cdot \kappa \nabla T - \sum_k \rho (q_k + \xi_k) \dot{\omega}_k \right) + \sum_k \frac{\partial p}{\partial X_k} \dot{\omega}_k \right) \equiv S. \quad (5)$$

### 3 Numerical methodology

In this section we discuss the numerical methodology used to integrate the low Mach number equations described above. Our basic discretization strategy is a fractional step approach based on a projection approximation. In this approach we integrate the equations for momentum, isotope abundances and enthalpy using a lagged approximation to the constraint. We then apply a discrete projection to the intermediate velocity computed in the first step to enforce the constraint. This basic fractional step algorithm is embedded in a hierarchical adaptive mesh refinement (AMR) algorithm. The version of the methodology presented here is an adaptation of the method presented by Day and Bell [11] for gaseous combustion. In the next subsection we describe the single-grid algorithm. We then discuss incorporation of that algorithm into an adaptive projection framework.

#### Single grid algorithm

The single grid algorithm is essentially a three-step process. First, we use an unsplit second-order Godunov procedure to predict a time-centered ( $t^{n+1/2}$ ) advection velocity,  $U^{\text{ADV},*}$ , using the cell-centered data at  $t^n$  and the lagged pressure gradient from the interval centered at  $t^{n-1/2}$ . The provisional field,  $U^{\text{ADV},*}$ , represents a normal velocity on cell edges analogous to a MAC-type staggered grid discretization of the Navier-Stokes equations (see [14], for example). However,  $U^{\text{ADV},*}$  fails to satisfy the time-centered divergence constraint. We apply a discrete projection by solving the elliptic equation

$$D^{\text{MAC}} \frac{1}{\rho^n} G^{\text{MAC}} \phi^{\text{MAC}} = D^{\text{MAC}} U^{\text{ADV},*} - \left( S^n + \frac{\Delta t^n}{2} \frac{S^n - S^{n-1}}{\Delta t^{n-1}} \right) \quad (6)$$

for  $\phi^{\text{MAC}}$ , where  $D^{\text{MAC}}$  represents a centered approximation to a cell-based divergence from edge-based velocities, and  $G^{\text{MAC}}$  represents a centered approximation to edge-based gradients from cell-centered data. The solution,  $\phi^{\text{MAC}}$ , is then used to define

$$U^{\text{ADV}} = U^{\text{ADV},*} - \frac{1}{\rho^n} G^{\text{MAC}} \phi^{\text{MAC}}.$$

$U^{\text{ADV}}$  is a second-order accurate, staggered-grid vector field at  $t^{n+1/2}$  that discretely satisfies the constraint (5), and is used for computing the time-explicit advective derivatives for  $U$ ,  $\rho h$  and  $\rho X_k$ .

In the next step of the algorithm we advance the advection-reaction-diffusion system for  $\rho h$  and  $\rho X_k$ . For the supernovae flames considered here, the nuclear burning occurs on a scale faster than the fluid dynamics. For that reason, we treat the reactions using a symmetric Strang-splitting approach so that the reactions can be treated with stiff ODE technology. We first advance the reactions terms  $\Delta t/2$  in time. We then advance the advection-diffusion part of the equation  $\Delta t$  in time followed by a second advancement of the reaction terms  $\Delta t/2$  in time.

The reaction part of the enthalpy and isotope equations are of the form

$$\frac{\partial X_k}{\partial t} = \dot{\omega}_k$$

and

$$c_p \frac{\partial T}{\partial t} = - \sum_k (q_k + \xi_k) \dot{\omega}_k$$

For the reaction phase,  $c_p$  changes with temperature and composition; however, because of the computational expense associated with computing  $c_p$  we have frozen its value for the integration of the ODE system. Numerical tests demonstrated that this simplification did not affect the computed deflagrations. As a result of this approximation, we do not use the updated temperature from the reaction step to update the enthalpy. Instead, we explicitly compute the change in enthalpy resulting from the change in isotope abundances and use this updated enthalpy to derive the correct temperature at the end of the reaction step.

In our implementation, we integrate the chemistry component using time-implicit backward difference methods, as implemented in **VODE** [6], a general-purpose stiff ODE integration software package. **VODE** utilizes adaptivity in order of accuracy and subcycled time-step selection so that an absolute error tolerance of  $10^{-16}$  in mass fractions is maintained throughout. Typically, the resulting scheme is between third and fifth order convergent in time.

After completing the first reaction step, we update the advection-diffusion component of the system. One numerical issue that must be addressed at this point is the nonlinearity of the enthalpy diffusion. The advection-diffusion part of the enthalpy equation may be written explicitly in terms of enthalpy diffusion

$$\frac{\partial \rho h}{\partial t} + \nabla \cdot U \rho h = \nabla \cdot \frac{\kappa}{c_p} \nabla h - \nabla \cdot \left( \sum_k \xi_k \frac{\kappa}{c_p} \nabla X_k \right) \quad (7)$$

We advance this equation using a linear Crank-Nicolson algorithm, but the coefficients  $\kappa$  and  $c_p$  vary with the solution over time and space. These variations may be incorporated into the linear scheme simply by using a predictor-corrector iteration (detailed below), where the coefficients at the new-time are re-evaluated between iterations. With a good initial guess for new-time  $\kappa$  and  $c_p$ , a single corrector iteration is sufficient to guarantee stability and second-order accuracy in time.

We begin the advection-diffusion step with the cell-centered data (denoted with a superscript  $n$ ) obtained from the initial chemistry advance. A second-order Godunov procedure is used to extrapolate the temperature and abundances at  $t^n$  to cell edges at  $t^{n+1/2} = t + \Delta t/2$ . The fluid density at the edges is computed using the relation,  $\rho = \sum_k \rho X_k$ , and the enthalpy,  $h$ , is computed from  $\rho$ ,  $T$ , and  $X_k$ . An explicit update for the new-time abundances at cell-centers,  $(\rho X_k)^{n+1}$  may be formed using the extrapolated edge states, and the projected advection velocity,  $U^{\text{ADV}}$ ,

$$(\rho X_k)^{n+1} = (\rho X_k)^n - \Delta t (\nabla \cdot U^{\text{ADV}} \rho X_k)^{n+1/2}. \quad (8)$$

A corresponding cell-centered value of density at  $t^{n+1}$  is then available using the expression  $\rho^{n+1} = \sum_k (\rho X_k)^{n+1}$ .

Next, we predict a preliminary  $t^{n+1}$  value of temperature,  $\tilde{T}$ , to be used in the initial estimates of the new-time transport coefficients. We employ a Crank-Nicolson discretization of the temperature equation with  $t^n$  values of  $\kappa$  and  $c_p$ .

$$\rho^{n+1/2} c_p^n \left( \frac{\tilde{T} - T^n}{\Delta t} + (U^{\text{ADV}} \cdot \nabla T)^{n+1/2} \right) = \frac{1}{2} (\nabla \kappa^n \nabla T^n + \nabla \kappa^n \nabla \tilde{T}) \quad (9)$$

where  $\rho^{n+1/2} = 1/2(\rho^{n+1} + \rho^n)$ . The new-time abundances and this preliminary temperature  $\tilde{T}$  are then used to evaluate provisional fluid properties  $(\kappa, c_p, \xi_k)^{n+1,*}$ . A predicted value of enthalpy  $h^{n+1,*}$  is then computed using

$$\begin{aligned} \frac{\rho^{n+1}h^{n+1,*} - \rho^n h^n}{\Delta t} &= (\nabla \cdot U^{\text{ADV}} \rho h)^{n+1/2} \\ &+ \nabla \cdot \frac{1}{2} \left[ \frac{\kappa^{n+1,*}}{c_p^{n+1,*}} \nabla h^{n+1,*} + \frac{\kappa^n}{c_p^n} \nabla h^n \right] \\ &- \nabla \cdot \frac{1}{2} \sum_k \left[ \left( \xi_k^{n+1,*} \frac{\kappa^{n+1,*}}{c_p^{n+1,*}} \right) \nabla X_k^{n+1} + \left( \xi_k^n \frac{\kappa^n}{c_p^n} \right) \nabla X_k^n \right]. \end{aligned} \quad (10)$$

We complete the predictor component of our advance algorithm by extracting an updated provisional temperature,  $T^{n+1,*}$ , using Newton's method from  $h^{n+1,*}$  and the  $X_k^{n+1}$  values computed earlier.

The corrector step begins with a re-evaluation of  $\kappa$  and  $c_p$  using  $T^{n+1,*}$  and  $X_k^{n+1}$ . The final enthalpy  $h^{n+1}$  is obtained by solving

$$\begin{aligned} \frac{\rho^{n+1}h^{n+1} - \rho^n h^n}{\Delta t} &= (\nabla \cdot U^{\text{ADV}} \rho h)^{n+1/2} \\ &+ \nabla \cdot \frac{1}{2} \left[ \frac{\kappa^{n+1}}{c_p^{n+1}} \nabla h^{n+1} + \frac{\kappa^n}{c_p^n} \nabla h^n \right] \\ &- \nabla \cdot \frac{1}{2} \sum_k \left[ \left( \xi_k^{n+1} \frac{\kappa^{n+1}}{c_p^{n+1}} \right) \nabla X_k^{n+1} + \left( \xi_k^n \frac{\kappa^n}{c_p^n} \right) \nabla X_k^n \right]. \end{aligned} \quad (11)$$

The temperature,  $T^{n+1}$ , is computed by once again inverting the equation of state for enthalpy, with  $h^{n+1}$  and  $X_k^{n+1}$ . The integration of the enthalpy and abundance equations is completed by again advancing the reaction part of the system  $\Delta t/2$  in time. This provides a complete update of the  $\rho$ ,  $h$ ,  $T$ , and  $X_k$ 's at the new time and allows us to evaluate the constraint on the velocity field,  $S^{n+1}$  at the new time.

The final step of basic integration step is to advance the velocity to the new time level. For this step we first obtain a provisional cell-centered velocity at  $t^{n+1}$  using a time-lagged pressure gradient,

$$\rho^{n+1/2} \frac{U^{n+1,*} - U^n}{\Delta t} + [(U^{\text{ADV}} \cdot \nabla)U]^{n+1/2} = -\nabla \pi^{n-1/2} + \rho^{n+1/2} \vec{g}.$$

At this point  $U^{n+1,*}$  does not satisfy the constraint. We apply an approximate projection to simultaneously update the pressure and to project  $U^{n+1,*}$  onto the constraint surface. In particular, we solve

$$L^\rho \phi = D(U^{n+1,*} + \frac{\Delta t}{\rho^{n+1/2}} G \pi^{n-1/2}) - S^{n+1} \quad (12)$$

for nodal values of  $\phi$ , where  $L^\rho$  is the standard bilinear finite element approximation to  $\nabla \cdot \frac{1}{\rho} \nabla$  with  $\rho$  evaluated at  $t^{n+1/2}$ . In this step,  $D$  is a discrete second-order operator that approximates the divergence at nodes from cell-centered data, and  $G = -D^T$  approximates a cell-centered gradient from nodal data. In the formulation,  $\phi$  satisfies Neumann boundary conditions at solid walls and inflow boundaries. At outflow boundaries, Dirichlet conditions are generated to suppress any tangential accelerations on the fluid leaving the domain. See Almgren et al. [2] for a more detailed discussion of projection issues. Nodal values for  $S^{n+1}$  for the solution of (12) are computed using a volume-weighted average of cell-centered values. Finally, we determine the new-time cell-centered velocity field from

$$U^{n+1} = U^{n+1,*} - \frac{\Delta t}{\rho^{n+1/2}} (G\phi - G\pi^{n-1/2})$$

and the new time-centered pressure from

$$\pi^{n+1/2} = \phi.$$

This completes the description of the time-advancement algorithm.

Before discussing the incorporation of this methodology in an adaptive mesh refinement algorithm, we note some of the properties of the algorithm. First, we emphasize that the temperature equation is used only in an auxiliary capacity in the algorithm. The energy is evolved using the numerically conservative discretized enthalpy equation, (10) and (11). As noted earlier, although the scheme rigorously satisfies conservation of mass and enthalpy, the evolution does not strictly maintain the equation of state at ambient pressure. Since the low Mach number asymptotics used to derive the governing equation show that the thermodynamic pressure only satisfies (1) to  $O(M^2)$ , relaxing the imposition of (1) is a reasonable way of dealing with the overdetermined system. To control the deviation from the equation of state we add a correction to constraint equation (5) based on approximating

$$\frac{f}{\gamma \rho \frac{\partial p}{\partial p}} \left( \frac{\partial p}{\partial t} + U \cdot \nabla p \right).$$

in the intermediate projection used to compute the velocity field required to evaluate convective derivatives. In this expression  $\gamma = c_p/c_v$  is the ratio of the two thermodynamic specific heats, and  $f$  is a constant relaxation factor. In particular, we approximate  $\partial p/\partial t$  by  $(p_{\text{amb}} - p_0)/\Delta t$ , where  $p_0$  is defined discretely from equation (1),  $p_{\text{amb}}$  is the specified ambient pressure, and  $U \cdot \nabla p$  is approximated with upwind differences using  $p_0$ . Thus, we are effectively adding a first-order approximation to the material derivative of  $p_0 - p_{\text{amb}}$  along streamlines. This forcing term prevents the solution from deviating an appreciable amount from the equation of state while maintaining the second-order accuracy of the overall scheme.

## Adaptive mesh refinement

In this section we present an overview of the adaptive projection algorithm. This framework, used in Day and Bell [11], was initially developed by Almgren et al. [1], and extended to low Mach number combustion by Pember et al. [23]. The discussion provides only an overview of the methodology. We refer the reader to the above papers for more details of the basic algorithm.

Our implementation of adaptive mesh refinement (AMR) is based on a sequence of nested grids with successively finer spacing in both time and space. In this approach, fine grids are formed by evenly dividing coarse cells by a refinement ratio,  $r$ , in each direction. Increasingly finer grids are recursively embedded in coarse grids until features of the solution are adequately resolved. An error estimation procedure based on user-specified criteria evaluates where additional refinement is needed and grid generation procedures dynamically create or remove rectangular fine grid patches as resolution requirements change.

The adaptive integration algorithm advances grids at different levels using time steps appropriate to that level, based on CFL considerations. The multi-level procedure can most easily be thought of as a recursive algorithm in which, to advance level  $\ell$ ,  $0 \leq \ell \leq \ell_{\text{max}}$ , the following steps are taken:

- Advance level  $\ell$  in time one time step,  $\Delta t^\ell$ , as if it is the only level. If  $\ell > 0$ , obtain boundary data using time-interpolated data from the grids at  $\ell - 1$ , as well as physical boundary conditions, where appropriate.
- If  $\ell < \ell_{\text{max}}$ 
  - Advance level  $(\ell + 1)$  for  $r$  time steps,  $\Delta t^{\ell+1} = \frac{1}{r} \Delta t^\ell$ , using level- $\ell$  data and the physical boundary conditions.
  - Synchronize the data between levels  $\ell$  and  $\ell + 1$ , and interpolate corrections to finer levels  $[\ell + 2, \dots, \ell_{\text{max}}]$ .

The adaptive algorithm, as outlined above, performs operations to advance the grids at each level independent of other levels in the hierarchy (except for boundary conditions) and then computes a correction

to synchronize the levels. Loosely speaking, the objective in this synchronization step is to compute the modifications to the coarse grid that reflect the change in the coarse grid solution due to the presence of the fine grid. More specifically, when solving on a fine grid, we supply Dirichlet boundary conditions from the coarse grid. This leads to a mismatch in the associated fluxes at the coarse-fine interface that is corrected by the synchronization.

For the adaptive projection methodology presented here there are three basic steps in the synchronization. First, the values obtained for  $U$ ,  $\rho X_k$  and  $\rho h$  are averaged from the fine grid onto the underlying coarse grid. We view the resulting data as defining a preliminary composite grid solution that is consistent between levels. We will denote this preliminary solution with a  $p$  superscript in the remainder of the section. To complete the synchronization we need to correct inconsistencies arising from the use of Dirichlet boundary conditions at coarse-fine boundaries. In particular, we compute increments to  $\rho X_k$  and  $\rho h$  that correct the flux mismatches at coarse-fine interfaces. Finally, we correct the velocity field to satisfy a divergence constraint over the composite grid system.

There are two components that contribute to flux mismatch. First,  $U^{\text{ADV}}$ , the edge-based advection velocity satisfies the constraint on the coarse level and the fine level separately. However, since we only satisfy the Dirichlet matching condition for  $\phi^{\text{MAC}}$  in (6), the value of  $U^{\text{ADV}}$  computed on the coarse level does not match the average value on the fine grid. We define the mismatch in advection velocities by

$$\delta U^{\text{ADV},\ell} = -U^{\text{ADV},\ell,n+1/2} + \frac{1}{r^2} \sum_{k=0}^{r-1} \sum_{\text{edges}} U^{\text{ADV},\ell+1,n+k+1/2}$$

along the coarse-fine boundary. We then solve the elliptic equation

$$D^{\text{MAC}} \frac{1}{\rho} G^{\text{MAC}} \delta e^\ell = D^{\text{MAC}} \delta U^{\text{ADV},\ell}$$

and compute

$$U^{\text{ADV},\ell,\text{corr}} = -\frac{1}{\rho} G^{\text{MAC}} \delta e^\ell$$

which is the correction needed for  $U^{\text{ADV}}$  to satisfy the constraint and matching conditions on the composite  $(\ell, \ell+1)$  grid hierarchy. This correction field is used to compute a modification to the advective fluxes for species and enthalpy that reflects an advection velocity field that satisfies the constraint on the composite grid.

The second part of the mismatch arises because the advective and diffusive fluxes on the coarse grid were computed without explicitly accounting for the fine grid, while on the fine grid the fluxes were computed using coarse-grid Dirichlet boundary data. We define the flux discrepancies

$$\delta F_{\rho h} = \Delta t^\ell \left( -F_{\rho h}^{\ell,n+1/2} + \frac{1}{r^2} \sum_{k=0}^{r-1} \sum_{\text{edges}} F_{\rho h}^{\ell+1,n+k+1/2} \right)$$

and

$$\delta F_{\rho X_k} = \Delta t^\ell \left( -F_{\rho X_k}^{\ell,n+1/2} + \frac{1}{r^2} \sum_{k=0}^{r-1} \sum_{\text{edges}} F_{\rho X_k}^{\ell+1,n+k+1/2} \right)$$

where  $F$  is the total (advective+diffusive) flux through a given interface prior to these synchronization operations. Since mass is conserved, corrections to density,  $\delta \rho^{\text{sync}}$ , on the coarse grid associated with mismatched advection fluxes may be computed explicitly

$$\delta \rho X_k^{\text{sync}} = -D^{\text{MAC}} (U^{\text{ADV},\text{corr}} \rho X_k)^{n+1/2} + \delta F_{\rho X_k}. \quad (13)$$

and  $\delta \rho^{\text{sync}} = \sum_k \delta \rho X_k^{\text{sync}}$ .



The synchronization correction for  $h$  is more complex because of the implicit discretization of diffusion. In particular, computing  $\delta h^{\text{sync}}$  requires solution of a linear system, since the flux mismatch contains implicit diffusion fluxes from the Crank-Nicolson discretization. To set up the synchronization, we first note that

$$\delta(\rho h)^{\text{sync}} = h^{n+1,p} \delta \rho^{\text{sync}} + \rho^{n+1} \delta h^{\text{sync}}.$$

Then, we have

$$\begin{aligned} \left( \rho^{n+1} - \frac{\Delta t}{2} \nabla \frac{\kappa^{n+1}}{c_p^{n+1}} \nabla \right) \delta h^{\text{sync}} &= -D^{\text{MAC}} (U^{\text{ADV,corr}} \rho h)^{n+1/2} + \delta F_{\rho h} \\ &+ \nabla \cdot \sum_k \xi_k(T^{n+1,p}) \left( \frac{\kappa^{n+1}}{c_p^{n+1}} \nabla \delta X_k^{\text{sync}} \right). \end{aligned} \quad (14)$$

The corrections  $\delta \rho^{\text{sync}}$ ,  $\delta \rho X_k^{\text{sync}}$ , and  $\delta \rho h^{\text{sync}}$  are added to the coarse field at level- $\ell$ , and interpolated to all finer levels. Finally, a new temperature field is computed using Newton's method on all affected levels.

A similar process is also used to generate a correction to the velocity field. However, the velocity flux correction must be projected to obtain the component satisfying the constraint that updates  $U$  and the component that updates  $\pi$ . At this point there are two additional corrections needed for the composite velocity field:

- A correction arising because the projection at level  $\ell + 1$  used Dirichlet data from level  $\ell$ , leading to a mismatch in normal derivative at coarse-fine boundaries
- The temperature and species adjustment in the first part of the synchronization leads to an increment in the computed  $S$  field.

Since the projection is linear, both of these corrections as well as the projection of the velocity flux correction can be combined into a single, multi-level node-based synchronization solve performed at the end of a coarse-grid time step.

We note that with the synchronization procedure outlined above the adaptive algorithm preserves the second-order accuracy and the conservation properties of the single-grid algorithm. The methodology has been implemented for distributed memory parallel processors using the **BoxLib** class libraries described by Rendleman et al. [25]. In this approach, grid patches are distributed to processors using a heuristic knapsack algorithm to balance the computational work developed by Crutchfield [9] (see also, Rendleman et al. [25]).

## 4 Results

In this section we present two sets of computational results. The first set of results presents comparisons of the low Mach number model with a comparable compressible code for one-dimensional flames at various densities. These examples serve to validate the low Mach number algorithm and quantify the errors associated with the low Mach number approximation. The second set of results describes the application of the methodology to simulation of Landau-Darrieus instability in two dimensions.

The numerical simulations were performed using the equation of state described by Timmes and Swesty [28] which computes the internal energy, pressure and thermodynamic derivatives (including the specific heats at constant volume and pressure) of these quantities as functions of temperature, density and the nuclear-species mass fractions. The values of the thermal conductivity,  $\kappa$ , are calculated using the procedure described by Timmes [27].

### Validation

The validation studies were performed by comparing one-dimensional laminar solutions tabulated in Dursi et al. [12] to  $^{12}\text{C}/^{24}\text{Mg}$  nuclear flames for several physical conditions. Each simulation was constructed in

the same way. A two-dimensional domain, periodic in one dimension, and with an inflow boundary condition on one face and an outflow condition on the opposite face is constructed. The simulations are initialized with For each case we initialize the domain with an interface separating  $^{12}\text{C}$  fuel and  $^{24}\text{Mg}$  ash. We specify density and temperature for the  $^{12}\text{C}$  and temperature for the  $^{24}\text{Mg}$ . For this specification, the temperature of the fuel must be below the initiation temperature for the reaction whereas the initial ash temperature must be high enough to ignite the flame. The ash density is computed from the equation of state so that pressure is constant in the domain, consistent with the low Mach number hypothesis. We specify inflow of the cold fuel at a fixed speed on the  $^{12}\text{C}$  side of the interface and specify outflow on the  $^{24}\text{Mg}$  side. The region of contact between the fuel and the ash is smoothed over a distance that is a small fraction of the size of the computational domain. The grid spacing is specified so that there are approximately 5 computational zones, at the coarsest level of refinement, in the flame.

The simulation proceeds with a single level of refinement until the initiation of the nuclear flame which is seen as a deviation of the temperature of the outflowing ash and a sharp increase in the energy generation rate. At that point, additional levels of refinement are added to the simulation until the speed of the nuclear flame and the flame shape converges. The simulation is then restarted using this computed constant speed to obtain a steady laminar solution.

To model the  $^{12}\text{C}/^{24}\text{Mg}$  reaction we used a single-step mechanism derived from Caughlan and Fowler [8]. This reaction has the form:

$$\begin{aligned}\dot{X}_{^{12}\text{C}}(t) &= -\frac{1}{12}R(T)\rho X_{^{12}\text{C}}^2(t) \\ \dot{T}(t) &= -Q\dot{X}_{^{12}\text{C}}(T)/c_p.\end{aligned}$$

where the rate of reaction,  $R(T)$ , is

$$R(T) = 4.27 \cdot 10^{26} \frac{T_{9,a}^{5/6}}{T_9^{3/2}} \exp \left\{ \frac{-84.165}{T_{9,a}^{1/3}} - 2.12 \cdot 10^{-3} T_9^3 \right\},$$

$T_9 = T/10^9$  K,  $T_{9,a} = T_9/(1 + 0.0396T_9)$ ,  $\rho$  is density (at the initial time), and  $Q$  is a constant. For the  $^{12}\text{C}/^{24}\text{Mg}$  reaction, the value of the specific energy release,  $Q$ , is taken to be  $5.57 \cdot 10^{17}$  erg/g. As noted above, the specific heat can be held constant with no apparent loss of accuracy. We neglect the effects of nuclear screening on this rate, as they are quite small for the conditions we consider.

Two  $^{12}\text{C}/^{24}\text{Mg}$  simulations with initial  $^{12}\text{C}$  density values of  $\rho = 2.5$  and  $5 \cdot 10^7$  g/cm<sup>3</sup>, both with a fuel temperature of  $10^7$  K were run. Measured laminar flame speeds differed by no more than .1% from those listed in Dursi et al [12]. Figure 1 shows the laminar flame solution for temperature, density and flow velocity for the case in which the initial  $^{12}\text{C}$  density is  $5 \cdot 10^7$  g/cm<sup>3</sup>. Because of differences in the ignition characteristics of these two approaches and the timing of when additional refinement levels are added, **FLASH** and the low Mach number code predict slightly different locations for where the flame stabilizes after ignition and subsequent refinement. For this reason we spatially shift the **FLASH** solutions for comparison to the low Mach number results. The shift is computed by minimizing the  $L_1$  of the difference in solution vectors for the laminar flames. As seen in Figure 1 the difference is largest near the steep change in temperature. The difference for temperature is in no case larger than approximately 1.25%; for density and flow velocity, the difference is no larger than 1%. We note that the shifts representing minor differences in where the flame stabilizes after ignition.

Finally, we make some additional remarks concerning the relative efficiency of the low Mach number method compared to the compressible methods. The low Mach number method in this paper and that used in **FLASH** have similar strategies for resolving spatial structures in the fluid flow. Therefore, they tend to result in similar resolutions in their spatial discretizations. Where they differ is in the time-step requirements. The time steps in a compressible method are limited by the need to obey the CFL constraint using as a velocity the speed of sound in the fluid; the low Mach number method has a similar CFL constraint, however it uses the fluid advection velocity. For the case considered in this section, the speed of sound is approximately  $5 \cdot 10^8$  cm/s, while a typical advective velocity is the laminar flame speed, which

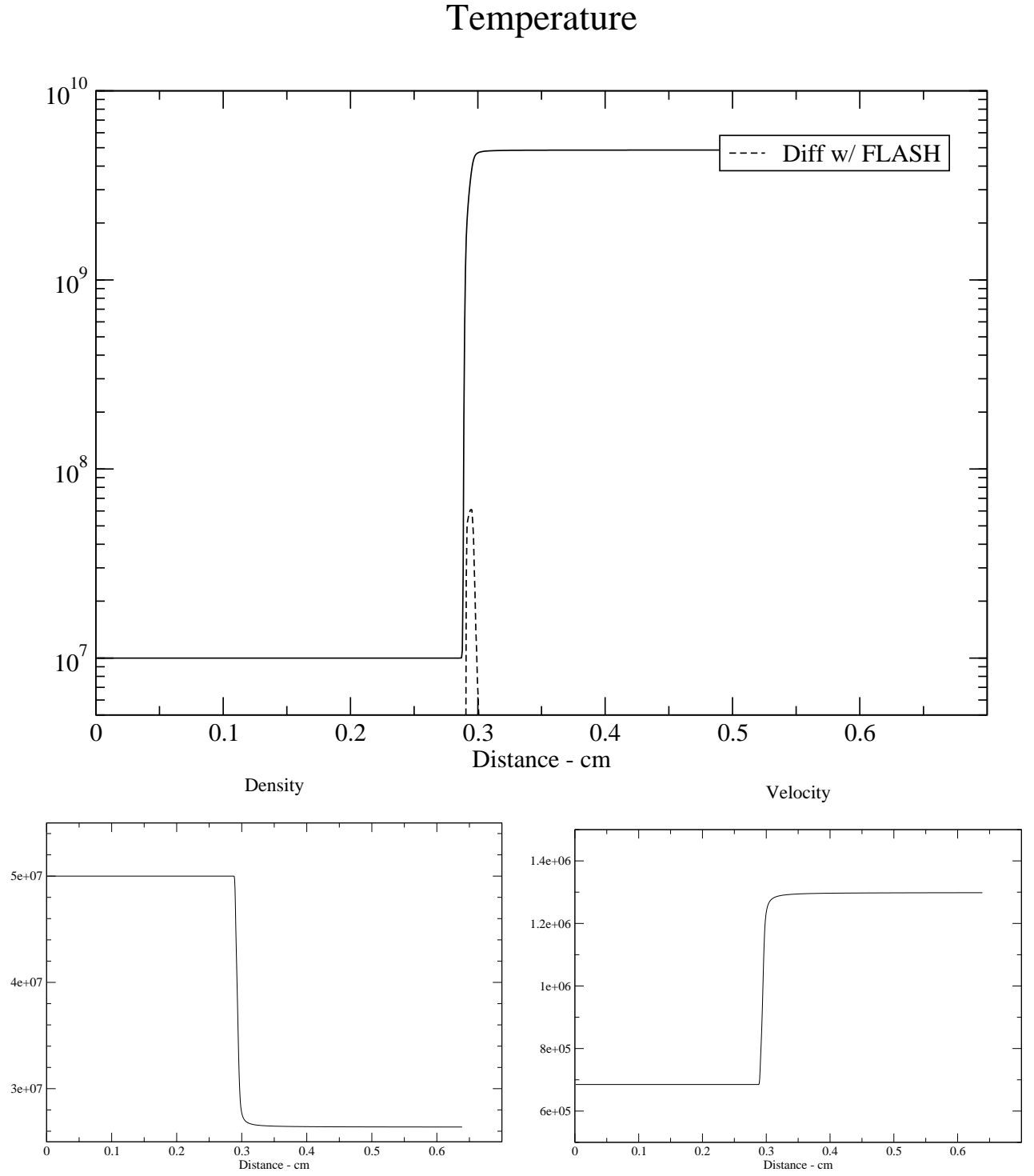


Figure 1: Laminar flame solution for  $\rho = 5 \cdot 10^7$  g/cm<sup>3</sup>,  $T = 10^7$  K. Shown are the solutions for density, speed, and temperature. The difference with the FLASH results from Dursi et al. [12] is indicated on the temperature result

is approximately  $6.82 \cdot 10^5$  cm/s. Thus, the low Mach number implementation requires roughly a factor of 1000 fewer time steps to model the same flow. For lower density flames, and flames that contain more than one species, this disparity can be even greater. For example, a flame consisting of 75%  $^{12}\text{C}$  and 25%  $^{16}\text{O}$  at a density of  $2.5 \cdot 10^7$  g/cm<sup>3</sup> has a ratio of sound speed to laminar speed of nearly 5000.

## Landau-Darrieus simulations

In this section we describe simulations designed to illustrate the Landau-Darrieus (LD) instability in a nuclear flame using direct numerical simulation. A perturbed initial planar inflow of  $^{12}\text{C}$  fuel impinges on a hot, lower density  $^{24}\text{Mg}$  ash. As above, the fuel burns in a single-step mechanism to form the ash. The initial perturbation is formed by shifting the laminar flame solution for the corresponding density, temperature, and mass fractions such that a fixed number of wavelengths of random phase and amplitude are contained in the domain.

Figure 2 illustrates the LD instability by showing the time history of velocity field. In this calculation the random perturbation of the initial planar laminar solution contained 30 frequencies of amplitude approximately 50 times the laminar flame thickness. The domain is  $2.56 \text{ cm} \times 1.28 \text{ cm}$  with  $1024 \times 512$  zones at the coarsest level of refinement. Cells with steep temperature gradients were refined up to two levels giving an effective computational domain of  $4096 \times 2048$  zones. The density of the  $^{12}\text{C}$  fuel is  $5 \cdot 10^7$  g/cm<sup>3</sup> and the inflow temperature is  $10^7$  K;  $^{12}\text{C}$  fuel is being passed in from the bottom into the ash that is at the top of the figure (i.e. the center of the star is above the top of the figure.) In this figure, the letters A and B mark two cusps that slowly coalesce to form a single LD cusp. This behavior was also seen in the LD calculation described next, and we conjecture that in periodic domains LD cusps will always coalesce until only one cusp remains. Figure 3 explains the appearance of the ‘searchlight’ features in Figure 2. The flow speed in the ash in the valleys between the cusps is higher than the flow speed in the ash above the peak of the LD cusp, except that the flow speed in the ash at the cusp is larger, decreasing quickly. The flow speed in the fuel is depressed the valleys between the cusps relative to the flow speed in the fuel below the LD cusps.

Figure 4 shows a well developed LD cusp for a simulation performed on a smaller domain using the same material parameters as in the previous example. In this case, only 5 frequencies were used to randomize the planar laminar solution. After about  $2\text{--}3 \mu\text{s}$  the details of the initial perturbations have disappeared and the LD cusps have coalesced. We continued to track the solution up to  $10 \mu\text{s}$ . Figure 5 shows the displacement in the stabilized LD cusp over a time range of approximately  $3 \mu\text{s}$ , indicating a increase in the laminar speed of 12, 210 cm/s, or about 1.8%. Over the time period  $3\text{--}10 \mu\text{s}$  the amplitude of the cusp decreases by .009 cm, which is approximately 10% of the extent of the cusp at  $t = 3 \mu\text{s}$ . The long time behavior of an isolated cusp is under investigation.

We note that the behavior of the flame undergoing the Landau-Darrieus instability at this density is considerable smoother than that shown in Niemeyer and Hillebrandt [21] for the same density. A large part of the difference is in the initialization—the flame in the present case was mapped onto the grid in steady state, and the low Mach number formulation means that no transient compression or rarefaction waves disturbed the flow ahead of the flame.

Several mechanisms have been proposed [15] that could give rise to an acceleration of the laminar flame speed in a Type Ia supernova. One part of some of these mechanisms is that the LD instability through the wrinkling in the flame surface, while not giving rise to turbulent motion, could give rise to sufficient flame speed acceleration to account for observed isotopic abundances and energy release. These calculations seem to indicate the LD instability by itself is insufficient to give rise to significant acceleration of the flame front.

## 5 Conclusions

The low Mach number numerical methods for gaseous combustion introduced by Day and Bell [11] has been successfully extended to account for non-ideal gas law equations of state. The method yields results that compares well with established compressible simulations (Dursi et al. [12]). The low Mach number method

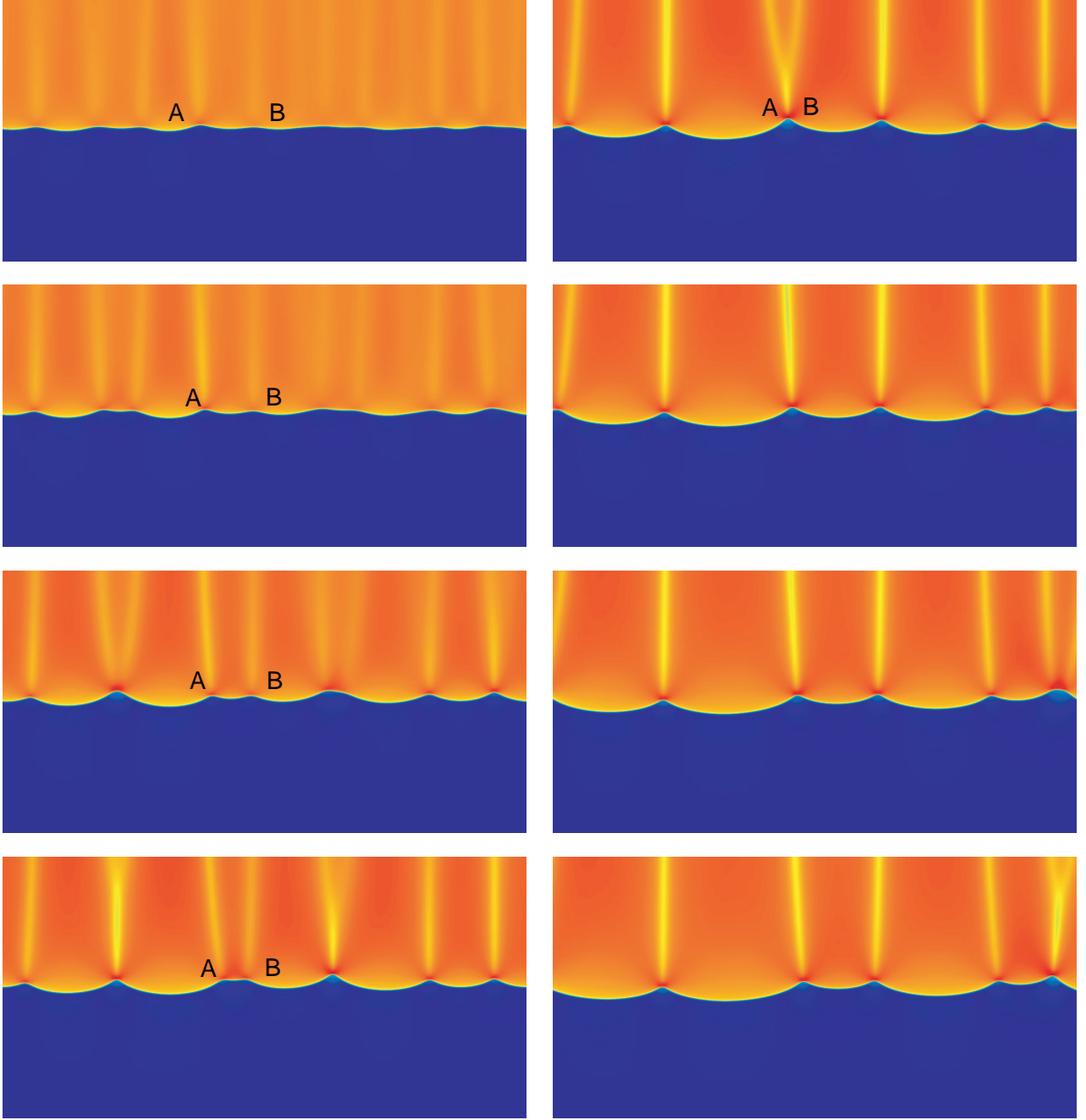


Figure 2: Time history of LD simulation, showing coalescence of LD peaks (e.g., A and B);  $\rho = 5 \cdot 10^7 \text{ g/cm}^3$  and  $T = 10^7 \text{ K}$ . Shown is vertical flow velocity. The ‘searchlights’ are regions of lower flow speed in the ash (see Figure 3.) Time increases down the left hand column from  $.78 \mu\text{s}$  and continues down the right column to  $3.4 \mu\text{s}$ .

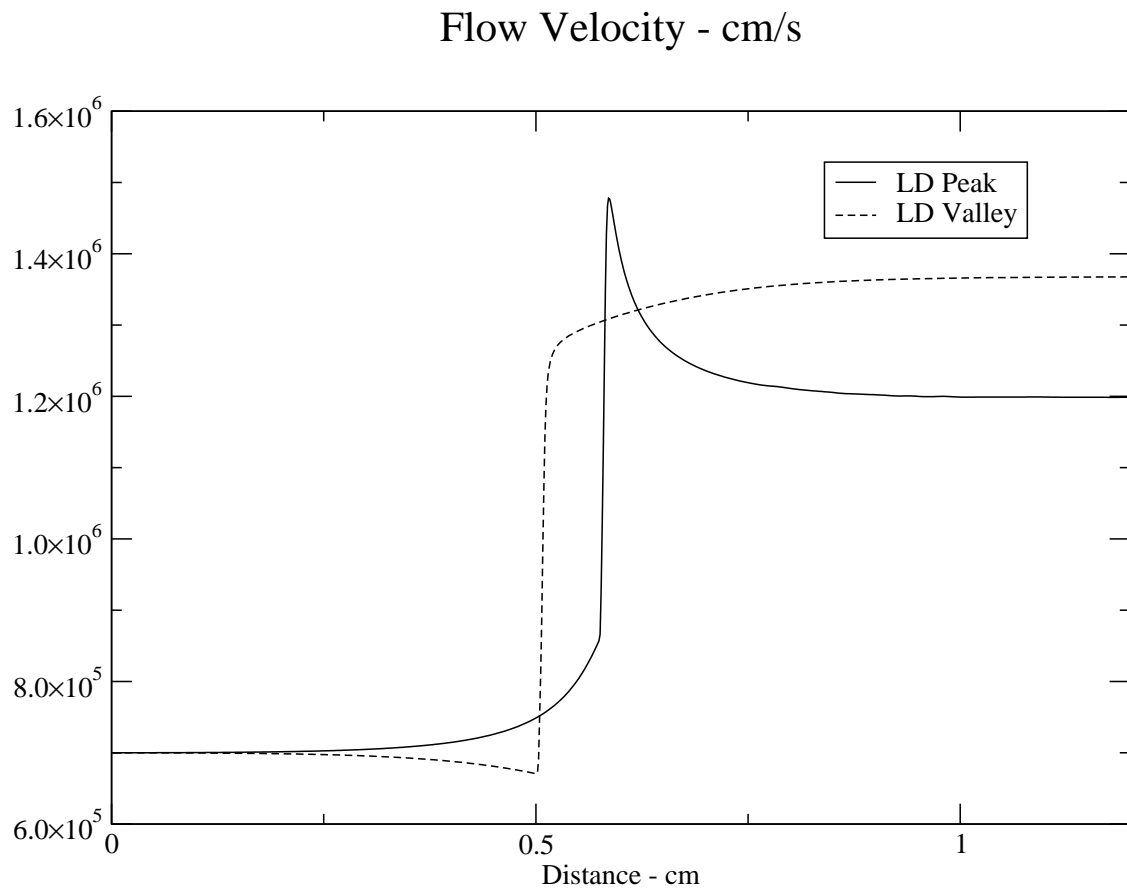


Figure 3: Flow velocity at peak of the LD cusp and valleys between the LD cusps

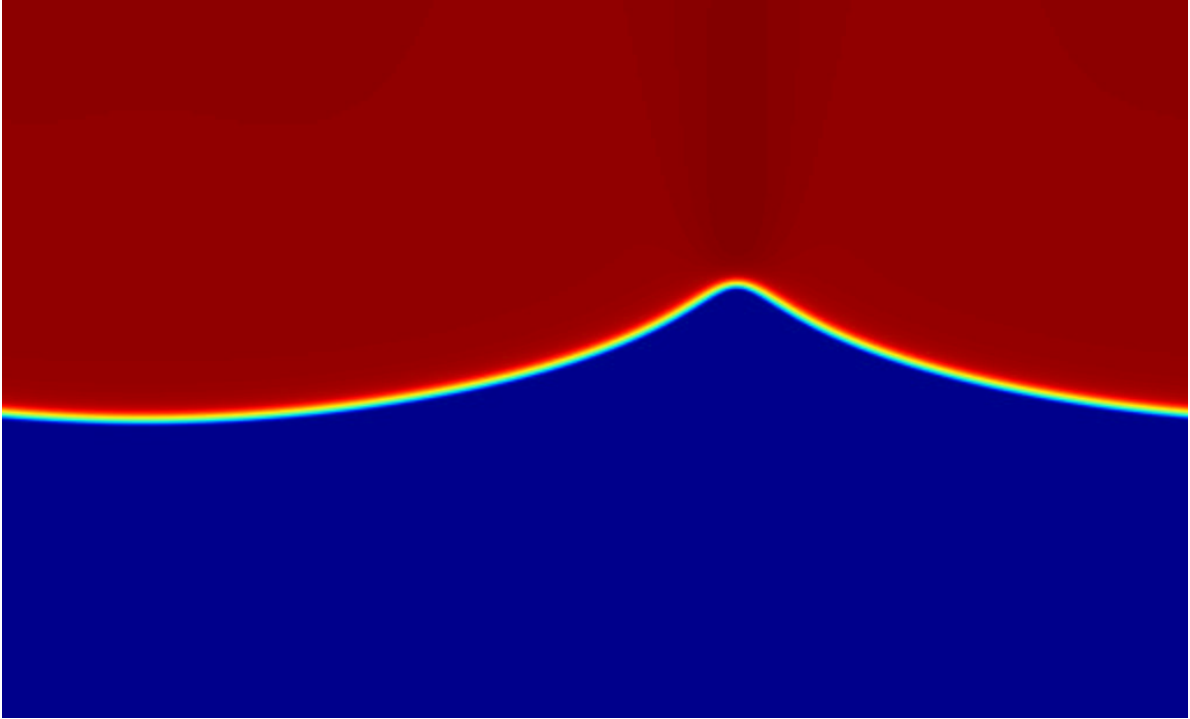


Figure 4: Landau Darrieus Cusp:  $^{12}\text{C}$ ,  $\rho = 5 \cdot 10^7 \text{ g/cm}^3$ ,  $T = 10^7 \text{ K}$ ;  $t = 10 \mu\text{s}$ .

enables new astrophysical problems to be explored, such as fully resolved instabilities at low-moderate densities; such problems are not tractable with a fully compressible code.

The program described in this paper will be used to conduct several sets of numerical experiments aimed at increasing our understanding of the microphysics of nuclear flames. Already, the program has been extended to handle more than one nuclear reaction, more than two isotopes, and three dimensions. This code will be used to perform a comprehensive examination of the phenomenology of two dimensional instabilities of the flame front. Later, the effects of Landau-Darrieus and Rayleigh-Taylor instabilities and their interaction with turbulence will be examined in three dimensions.

## Acknowledgments

The work of Bell, Day and Rendleman was supported by the Applied Mathematics Program of the DOE Office of Mathematics, Information, and Computational Sciences under the U.S. Department of Energy under contract No. DE-AC03-76SF00098. Woosley and Zingale were supported by the Scientific Discovery through Advanced Computing (SciDAC) program of the DOE, grant number DE-FC02-01ER41176 to the Supernova Science Center/UCSC. We thank F. X. Timmes for making his equation of state and conductivity routines available online.

## References

- [1] A. S. Almgren, J. B. Bell, P. Colella, L. H. Howell, and M. Welcome. A conservative adaptive projection method for the variable density incompressible Navier-Stokes equations. *J. Comput. Phys.*, 142:1–46, 1998.

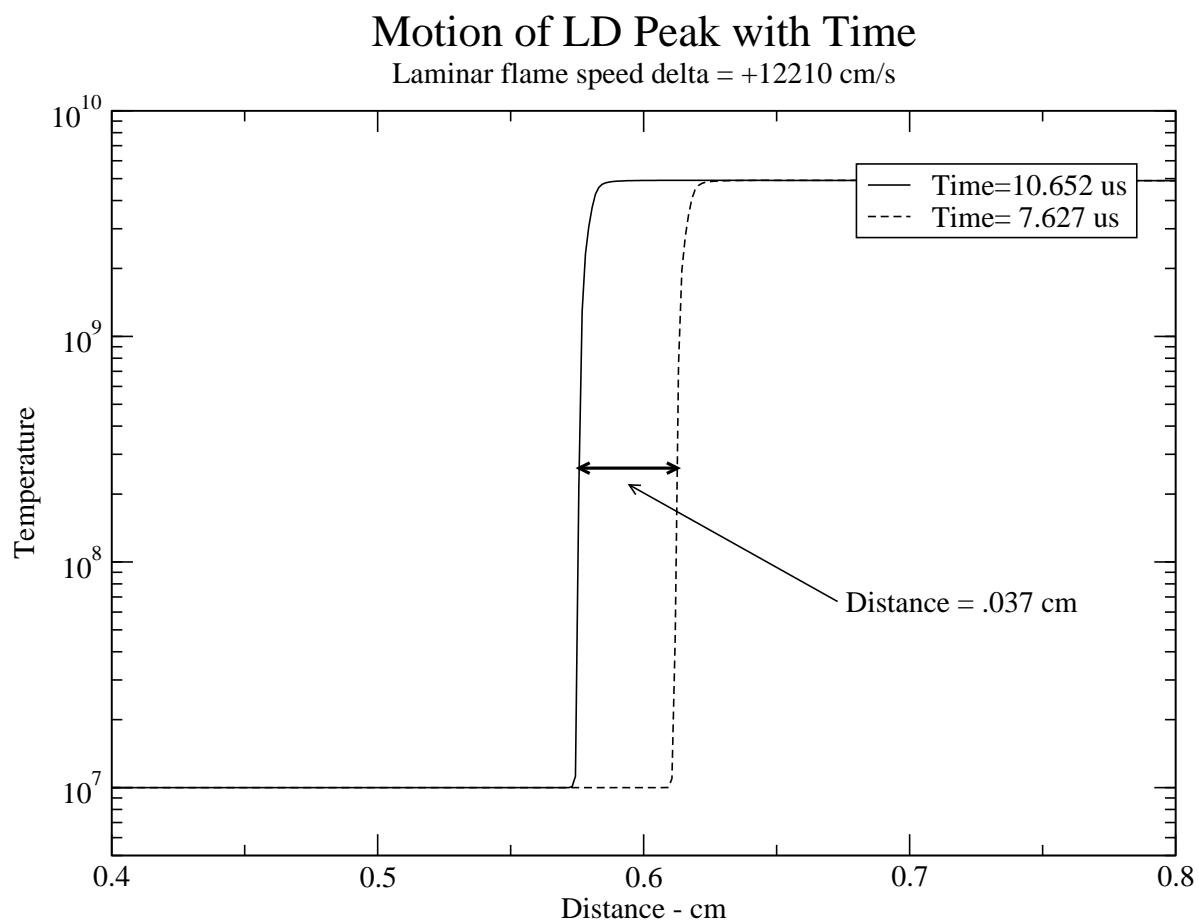


Figure 5:



- [2] A. S. Almgren, J. B. Bell, and W. Y. Crutchfield. Approximate projection methods: Part I. Inviscid analysis. *SIAM J. Sci. Comput.*, 22(4):1139–59, 2000.
- [3] J. B. Bell, N. J. Brown, M. S. Day, M. Frenklach, J. F. Grcar, and S. R. Tonse. The dependence of chemistry on the inlet equivalence ratio in vortex-flame interactions. *Proc. Combust. Inst.*, 28:1933–1939, 2000.
- [4] J. B. Bell, M. S. Day, J. F. Grcar, and M. J. Lijewski. Numerical simulation of premixed turbulent methane combustion. Technical Report LBNL-49331, Lawrence Berkeley National Laboratory, 2002. submitted to Proceedings of the Combustion Institute.
- [5] S. I. Blinnikov and P. V. Sasorov. Landau-Darrieus instability and the fractal dimension of flame fronts. *Phys. Rev. E*, 53:4827–4841, May 1996.
- [6] P. N. Brown, G. D. Byrne, and A. C. Hindmarsh. VODE: A variable coefficient ode solver. *SIAM J. Sci. Stat. Comput.*, 10:1038–1051, 1989.
- [7] A. C. Calder, B. Fryxell, T. Plewa, R. Rosner, L. J. Dursi, V. G. Weirs, T. Dupont, H. F. Robey, J. O. Kane, B. A. Remington, R. P. Drake, G. Dimonte, M. Zingale, F. X. Timmes, K. Olson, P. Ricker, P. MacNeice, and H. M. Tufo. On Validating an Astrophysical Simulation Code. *Astrophysical Journal Supplement*, 143:201–229, November 2002.
- [8] G. R. Caughlan and W. A. Fowler. Thermonuclear reaction rates V. *Atomic Data and Nuclear Data Tables*, 40(2):283–334, 1988. see also <http://www.phy.ornl.gov/astrophysics/data/cf88/index.html>.
- [9] William Y. Crutchfield. Load balancing irregular algorithms. Technical Report UCRL-JC-107679, Lawrence Livermore National Laboratory, July 1991.
- [10] G. Darrieus. Propagation d’un front de flamme. In *La Technique Moderne*, France, 1938.
- [11] M. S. Day and J. B. Bell. Numerical simulation of laminar reacting flows with complex chemistry. *Combust. Theory Modelling*, 4(4):535–556, 2000.
- [12] L. J. Dursi, M. Zingale, A. C. Calder, B. Fryxell, F. X. Timmes, N. Vladimirova, R. Rosner, A. Caceres, D. Q. Lamb, K. Olson, P. M. Ricker, K. Riley, A. Siegel, and J. W. Truran. The Response of Astrophysical Thermonuclear Flames to Curvature and Stretch. *Astrophysical Journal Supplement*, 2003. submitted.
- [13] B. Fryxell, K. Olson, P. Ricker, F. X. Timmes, M. Zingale, D. Q. Lamb, P. MacNeice, R. Rosner, J. W. Truran, and H. Tufo. FLASH: An Adaptive Mesh Hydrodynamics Code for Modeling Astrophysical Thermonuclear Flashes. *Astrophysical Journal Supplement*, 131:273–334, November 2000.
- [14] F. H. Harlow and J. E. Welch. Numerical calculation of time-dependent viscous incompressible flow of fluids with free surfaces. *Physics of Fluids*, 8:2182–2189, 1965.
- [15] Wolfgang Hillebrandt and Jens C. Niemeyer. Type Ia supernova explosion models. *Annu. Rev. Astron. Astrophys.*, 38:191–230, 2000.
- [16] Alexei M. Khokhlov. Propagation of turbulent flames in supernovae. *Astrophysical Journal*, 449:695, 1995.
- [17] Rudolf Kippenhahn and Alfred Weigert. *Stellar Structure and Evolution*. Springer Verlag, 1992.
- [18] L. D. Landau. On the theory of slow combustion. *Acta Physicochimica, URSS*, 19:77, 1944.

- [19] A. Majda and J. A. Sethian. The derivation and numerical solution of the equations for zero Mach number combustion. *Combust. Sci. Technol.*, 42:185–205, 1985.
- [20] Jens C. Niemeyer, W. K. Busche, and G. R. Ruetsch. Small-scale interaction of turbulence with thermonuclear flames in type ia supernovae. *Astrophysical Journal*, 524:290, 1999.
- [21] Jens C. Niemeyer and Wolfgang Hillebrandt. Microscopic instabilities of nuclear flames in type ia supernovae. *Astrophysical Journal*, 452:779–784, 1995.
- [22] Jens C. Niemeyer and Wolfgang Hillebrandt. Microscopic and macroscopic modeling of thermonuclear burning fronts. In P. Ruiz-Lapuente, R. Canal, and R. Isern, editors, *Thermonuclear Supernovae*. Dordrecht:Kluwer, 1997.
- [23] R. B. Pember, L. H. Howell, J. B. Bell, P. Colella, W. Y. Crutchfield, W. A. Fiveland, and J. P. Jessee. An adaptive projection method for unsteady, low-Mach number combustion. *Comb. Sci. Technol.*, 140:123–168, 1998.
- [24] R.G. Rehm and H.R. Baum. The equations of motion for thermally driven buoyant flows. *N.B.S.J.Res.*, 83:297–308, 1978.
- [25] Charles A. Rendleman, Vincent E. Beckner, Mike Lijewski, William Y. Crutchfield, and John B. Bell. Parallelization of structured, hierarchical adaptive mesh refinement algorithms. *Computing and Visualization in Science*, 3(3):147–157, 2000.
- [26] F. X. Timmes and S. E. Woosley. The conductive propagation of nuclear flames i. degenerate C+O and O+Ne+Mg white dwarfs. *Astrophysical Journal*, 396:649–667, September 1992.
- [27] Frank X. Timmes. The physical properties of laminar helium deflagrations. *Astrophysical Journal*, 528:913, 2000.
- [28] Frank X. Timmes and F. Douglas Swesty. The accuracy, consistency, and speed of an electron-positron equation of state based on table interpolation of the helmholtz free energy. *Astrophysical Journal Supplement*, 126:501–516, 2000.